

Submitted to ApJ January 2007

Particle Acceleration in Supernova Remnants and the Production of Thermal and Nonthermal Radiation

Donald C. Ellison

*Physics Department, North Carolina State University, Box 8202, Raleigh, NC 27695, U.S.A.,
don_ellison@ncsu.edu*

Daniel J. Patnaude

*Harvard Smithsonian Center for Astrophysics, 60 Garden St., Cambridge, MA 02138, U.S.A.,
patnaude@head.cfa.harvard.edu*

Patrick Slane

*Harvard Smithsonian Center for Astrophysics, 60 Garden St., Cambridge, MA 02138, U.S.A.,
slane@cfa.harvard.edu*

Pasquale Blasi

*INAF/Istituto Nazionale di Astrofisica, Osservatorio Astrofisico di Arcetri, Largo E. Fermi 5,
I-50125, Firenze, Italy, blasi@arcetri.astro.it*

Stefano Gabici

*Max-Planck-Institut fuer Kernphysik, Saupfercheckweg 1, 69117 Heidelberg, Germany
Stefano.Gabici@mpi-hd.mpg.de*

ABSTRACT

Energetic particle production in supernova remnants (SNRs) through diffusive shock acceleration has long been suggested as a mechanism by which the bulk of cosmic rays with energies less than $\sim 10^{15}$ eV are formed. If highly efficient, this process can have a significant effect on the X-ray emission from SNRs as well as their dynamical evolution. Here we investigate the expected modification to the thermal X-ray emission from the forward shock region of young SNRs in which efficient particle acceleration is occurring. Using hydrodynamical simulations for a range of ambient density and magnetic field values, we produce spectra for both the thermal and nonthermal emission components of the postshock gas. For a given ambient density and explosion energy, we find that the position of the forward shock at a given age is a strong function of the acceleration efficiency, providing a strong signature of cosmic ray production. Using an

approximate treatment for the ionization state of the plasma, appropriate for the range of models considered, we investigate the effects of slow vs. rapid heating of the postshock electrons on the ratio of thermal to nonthermal X-ray emission at the forward shock. We also investigate the effects of magnetic field strength on the observed spectrum for efficient cosmic ray acceleration. The primary effect of a large field, aside from an overall increased flux for higher fields, is a considerable flattening of the nonthermal spectrum in the soft X-ray band. Spectral index measurements from X-ray observations may thus be used as indicators of the postshock magnetic field strength. The predicted gamma-ray flux from inverse-Compton (IC) scattering and neutral pion (π^0) decay is strongly affected by the ambient conditions. For the particular parameters used in our examples, the IC emission at $E \sim 1$ TeV exceeds that from π^0 decay, although at lower energies of several GeV and at higher energies $> \text{TeV}$, this trend is reversed for cases of high ambient density. More importantly, for high magnetic fields, we find that radiation losses, combined with evolutionary effects, produce a steepening of the electron spectrum over a wide energy range and results in a severe flattening of the IC spectral shape, making it more difficult to differentiate from that due to pion decay.

Subject headings: Supernova Remnants, cosmic rays, shock acceleration, X-ray emission, MHD turbulence

1. INTRODUCTION

The production of relativistic electrons is beyond doubt in young supernova remnants (SNRs) and it is believed that remnants simultaneously produce relativistic ions, i.e., cosmic rays (CRs), although the evidence for this is less direct. SNRs also produce thermal X-ray line emission, and this contains a vast amount of information about the composition and ionization state of the gas that is absent in continuum emission. The premise of this paper is that shocks in SNRs accelerate ions *efficiently* via diffusive shock acceleration (DSA) and that this particle acceleration influences the evolution of the remnant, and in particular, the *thermal* X-ray emission, in important and predictable ways. In the current era of high resolution, high energy astronomy, it has become critical that self-consistent, broad-band models of SNR radiation under the assumption of efficient particle acceleration be developed. Towards this goal, we present a self-consistent model of thermal and non-thermal X-ray emission in SNRs. The model includes the acceleration and feedback of CRs on the SNR evolution and on the structure and thermal properties of the shocked gas in the interaction region between the forward and reverse shocks. In this paper, the first in a series, we investigate the dynamical and spectral evolution of the forward shock region only, where the vast majority of the cosmic ray production is expected to occur. In subsequent papers we will treat results for the ejecta component and provide a more complete treatment of the ionization within the SNR.

Radiation from shell-like SNRs consists of thermal emission from shock-heated gas and non-thermal emission from shock accelerated particles.¹ X-rays consist of a thermal component which contains emission from both shock-heated ejecta and circumstellar medium (CSM). Since the ejecta and CSM generally have very different compositions, the separation of these two components observationally is often possible. In this paper we concentrate on thermal emission from the shocked circumstellar medium (CSM) material in order to highlight the physical effects we wish to emphasize without the additional complications introduced by the complex composition and ionization state of the shocked ejecta.

A number of SNRs also show non-thermal X-ray emission and some (e.g., RX J1713.7-3946) even show non-thermal X-rays with no discernable thermal component (Slane et al. 1999). Non-thermal X-rays are believed to be synchrotron radiation from shock accelerated TeV electrons. Radio emission has long been observed from SNRs in the form of synchrotron radiation from relativistic electrons accelerated at the outer blast wave. In addition, higher energy photons at GeV–TeV energies (either inverse-Compton radiation from electrons or pion-decay emission from ions) have been detected from some remnants, particularly by HESS and CANGAROO (e.g., Aharonian et al. 2004; Tanimori et al. 1998) and now MAGIC (e.g., Albert et al. 2006), and soon VERITAS (LeBohec et al. 2006).

If the particle acceleration process is efficient DSA, as is now becoming more generally accepted, the nonlinear theory makes clear predictions for the underlying electron and ion spectra which produce the broad-band photon emission (e.g., Jones & Ellison 1991; Baring et al. 1999). While a number of authors have calculated the continuum emission from synchrotron, inverse-Compton, and pion-decay emission (e.g., Ellison, Slane, & Gaensler 2001; Berezhko, Ksenofontov, & Völk 2002), there have been, to our knowledge, no self-consistent calculations of the thermal and non-thermal X-ray emission in SNRs. The most complete attempt to do this that we are aware of is that of Decourchelle, Ellison, & Ballet (2000), who used a self-similar analytic model of the SNR hydrodynamics with input from a nonlinear calculation of DSA, which modified the thermal properties of the interaction region. This model did not, however, self-consistently calculate the SNR evolution or include the non-thermal synchrotron component self-consistently. Earlier work by Dorfi & Bohringer (1993) (see also Chevalier 1983; Heavens 1984; Boulares & Cox 1988), clearly showed the importance of including nonlinear particle acceleration in SNR models but did not attempt self-consistent calculations of thermal and non-thermal emission in the X-ray band.

In this paper, we have incorporated a non-equilibrium ionization (NEI) model of X-ray line and continuum emission into a spherically symmetric hydrodynamic simulation of SNRs. The hydrodynamics include efficient, nonlinear DSA and the effects of this particle acceleration on the shocked thermal plasma, as well as on the structure and evolution of the remnant. Our model includes: (i) shock heating at both the forward and reverse shocks; (ii) nonlinear particle acceleration at the forward shock; (iii) a consistent modeling of the evolution of the material in the

¹We do not consider emission from heated dust or from a compact object in this paper.

interaction region between the forward and reverse shocks; and (iv) the calculation of full electron and proton distribution functions which allow the non-thermal synchrotron contribution to the X-ray emission to be determined self-consistently with the thermal emission. The thermal emission is calculated for an optically thin plasma in nonequilibrium ionization with negligible cooling.

Efficient DSA predicts greater compression ratios and lower plasma temperatures than produced in shocks with little or no particle acceleration. These two effects will influence the X-ray emission from the shocked CSM where DSA is expected to be efficient. The changes in SNR evolution produced by efficient DSA at the forward shock (FS) modify the thermal emission from the shocked ejecta even if DSA is absent at the reverse shock (RS). While these changes may be small, the non-thermal synchrotron emission from the FS may produce large changes in the observed ejecta emission through line-of-sight effects even without DSA at the RS.

In § 2 we outline our model. We use the results from time-dependent hydrodynamical models with efficient DSA as inputs to a NEI calculation. We discuss our approach to the problem of nonequilibrium ionization in § 2 as well. We present our results in § 3 and discuss the quantitative and qualitative effects of DSA on thermal X-ray emission in § 4. Finally, in § 4 we present and discuss the limitations of our approach and present possible solutions to these limitations as well as future directions.

2. CR-HYDRO MODEL WITH X-RAY EMISSION

Our model consists of three main parts: (i) the hydrodynamics of the SNR coupled to nonlinear DSA (our so-called CR-hydro model); (ii) a calculation of X-ray synchrotron emission from shock accelerated electrons; and (iii) a non-equilibrium ionization (NEI) calculation of thermal X-ray emission using the output of the CR-hydro model.

2.1. CR Hydrodynamics and Electron Spectra

We calculate the hydrodynamic evolution of a SNR with a radially symmetric model described in detail in Ellison & Cassam-Chenaï (2005) and references therein. For reference, we reproduce the geometry of the simulation in Figure 1. The current model couples efficient DSA to the hydrodynamics and differs from that described in Ellison & Cassam-Chenaï (2005) in that we have replaced the algebraic model of DSA of Berezhko & Ellison (1999) with the more accurate semi-analytic model of Blasi, Gabici, & Vannoni (2005).² Given an injection parameter, χ_{inj} (this is ξ in equation (25) in Blasi et al. 2005), the semi-analytic model solves the nonlinear DSA problem

²The work of Blasi et al. (2005), which is based on the approximate solution of Blasi (2002, 2004), showed that multiple solutions could be eliminated by relating the injection momentum to the thermal momentum of the shocked particles. Recently, an exact solution for arbitrary conditions has been presented by Amato & Blasi (2005, 2006).

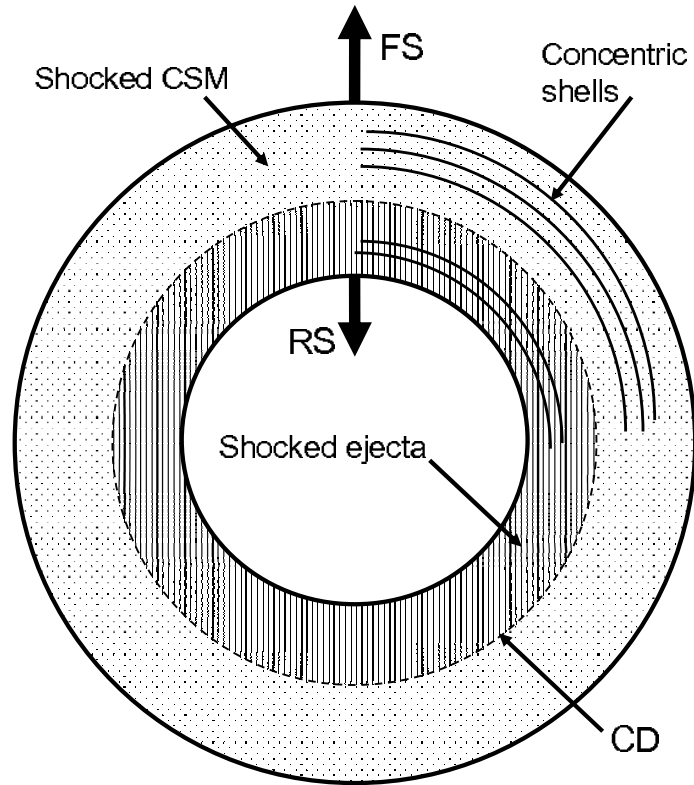


Fig. 1.— Spherical SNR model showing the forward shock (FS), reverse shock (RS), and contact discontinuity (CD). The CD separates the shocked circumstellar medium (CSM) from the shocked ejecta. The RS is an inward directed shock even though it moves outward during the early stages of the SNR evolution. As the forward and reverse shocks overtake new material, the cosmic-ray population is determined in concentric shells (indicated schematically) that evolve as the SNR ages.

Table 1: Parameters for models shown in Figures 2–5 and Figures 7–12. In all models $M_{\text{ej}} = 1.4 M_{\odot}$, $t_{\text{SNR}} = 500 \text{ yr}$, $D_{\text{SNR}} = 1 \text{ kpc}$, and an exponential ejecta density profile is used. For all models except D2, $E_{\text{SN}} = 10^{51} \text{ erg}$. For D2, $E_{\text{SN}} = 1.4 \times 10^{51} \text{ erg}$.

Model ^a	n_{H} [cm^{-3}]	B_0 [μG]	χ_{inj}	ϵ_{rel} [%]	$\epsilon_{\text{esc}}^{\text{b}}$ [%]	$r_{\text{tot}}^{\text{c}}$	B_2^{d} [μG]	R_{FS}^{e} [pc]	$(\frac{\text{synch}}{\text{therm}})^{\text{f}}$	$\frac{\text{pion}}{\text{IC}} _{1\text{TeV}}$
A1	0.1	15	6	0	0	4	60	5.0	0	...
A2	0.1	15	3.91	10	1.6	4.3	65	4.9	4.68	0.048
A3	0.1	15	3.62	50	16	6.5	98	4.7	13.8	0.20
B1	0.01	15	3.58	36	7.5	5.5	83	6.6	3900	0.010
B2 ^g	0.1	15	3.73	36	9.4	5.5	83	4.8	13.5	0.077
B3	1	15	3.82	36	11	5.6	84	3.4	0.44	0.65
C1	0.1	3	3.752	36	11	5.6	17	4.9	1.5	0.027
C2 ^g	0.1	15	3.73	36	9.4	5.5	83	4.8	13.5	0.077
C3	0.1	60	3.2	36	19	5.2	310	4.7	22.7	1.1
D1	0.1	15	3.3	63	23	7.7	116	4.6
D2 ^h	0.1	15	3.3	64	24	7.8	120	5.0

^aModels A, B, and C are shown in Figures 8, 9, and 10, respectively. Models D1 and D2 are shown in Figure 2

^bThis is the percent of energy flux which escapes upstream of the FS at t_{SNR} .

^cThis is the FS compression ratio at t_{SNR} .

^dThis is the magnetic field immediately behind the FS at t_{SNR} .

^eRadius of the FS at t_{SNR} .

^fThese values are summed over the 0.4 – 10 keV energy range and are for the Coulomb heating case.

^gModels B2 and C2 are identical.

^hThis model has $E_{\text{SN}} = 1.4 \times 10^{51} \text{ erg}$ and should be compared to model A1 with $E_{\text{SN}} = 1 \times 10^{51} \text{ erg}$.

at each time-step of the hydro simulation using the shock speed, shock radius, ambient density and temperature, and ambient magnetic field determined in the simulation. With the accelerated particle distribution, an effective ratio of specific heats is calculated and used in the hydrodynamic equations, completing the coupling between the two (see Ellison, Decourchelle, & Ballet 2004, for a fuller discussion).

At any given time, the CR-hydro calculation returns a set of concentric shells of shocked material, both shocked ejecta and shocked CSM, separated by a contact discontinuity (CD). The hydrodynamics are calculated in Lagrangian mass coordinates so the amount of material in a mass shell remains constant as the volume of a shell is adjusted in response to the changing pressure. New shells of shocked gas are added as the forward and reverse shocks overtake fresh material.

Particle acceleration influences the SNR evolution since relativistic particles produce less pressure for a given energy density than do non-relativistic particles. In addition, particles at the maximum energy “escape” upstream from the shock system during acceleration and carry away energy and pressure, thus further softening the equation of state. This escape is included implicitly in the semi-analytic DSA calculation (see Berezhko & Ellison 1999) and is distinct from the diffusion of particles into and out of a particular shell. Since we use Lagrangian coordinates we ignore the diffusion of particles into and out of a shell after the initial acceleration. This is a reasonable approximation for low energy particles, but becomes less accurate as the particle energy and diffusion lengths increase.

The softening of the equation of state means that compression ratios well in excess of four can be produced in non-radiative, collisionless shocks further modifying the SNR evolution (e.g., Eichler 1984). The nature of nonlinear DSA, on the other hand, uniquely predicts that a concave superthermal particle spectrum, hardening at higher momenta, will be produced. Here the energy that goes into the highest momenta particles comes from the shock-heated thermal population. Thus, the fundamental changes that occur with efficient DSA are larger compression ratios, lower temperatures of the shocked gas (compared to shocks without efficient DSA), and concave energetic particle spectra.³

An important question for SNRs is whether or not particle acceleration occurs at the RS. While it is likely that, due to expansion, the magnetic field interior to the RS is too small to allow acceleration, there have been reports of radio (Gotthelf et al. 2001; DeLaney et al. 2002) and even X-ray synchrotron emission (Rho et al. 2002) at the RS in some SNRs. As discussed in Ellison, Decourchelle, & Ballet (2005), confirmation of particle acceleration at the RS will indicate strong magnetic field amplification and will have far-reaching consequences. For now, however, we assume there is no appreciable acceleration at the RS, but note that the large changes in the

³The concave curvature in the superthermal portions of the spectra in the middle panel of Figure 5 is present but small. The curvature becomes more pronounced with greater acceleration efficiency (see Fig. 1 in Ellison, Berezhko, & Baring 2000) and may actually have been detected in SNR spectra (e.g., Reynolds & Ellison 1992; Jones et al. 2003; Allen et al. 2005).

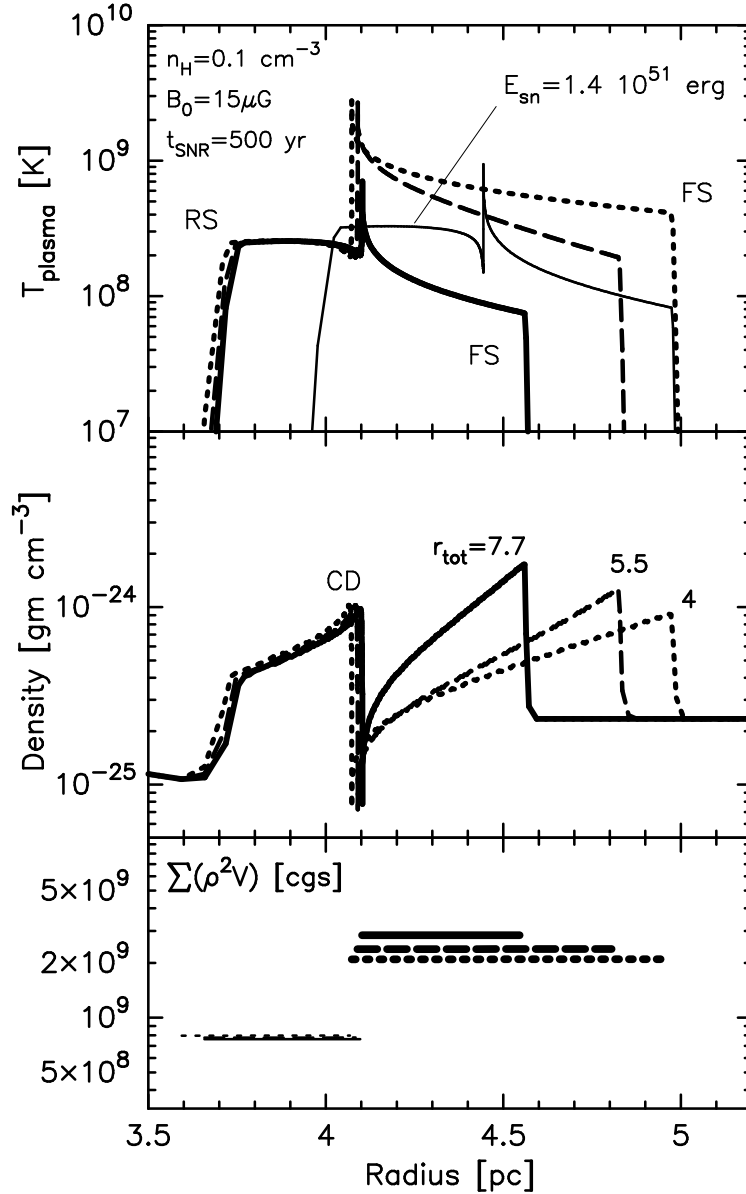


Fig. 2.— The top and middle panels show radial distributions of the plasma temperature and density for SNRs with different shock acceleration efficiencies at the FS. The bottom panel shows $\sum \rho^2 V$ where each horizontal line indicates the value summed over the shocked ejecta or shocked CSM regions. In all panels, the heavy-weight solid curves (model D1 in table) are for efficient DSA ($\epsilon_{\text{rel}} \simeq 63\%$), the dashed curves (model B2) are for moderate DSA ($\epsilon_{\text{rel}} \simeq 36\%$), and the dotted curves (model A1) are for test-particle ($\epsilon_{\text{rel}} \simeq 0$). In the top panel, the light-weight solid curve (model D2) is an efficient acceleration case ($\epsilon_{\text{rel}} \simeq 63\%$) where E_{SN} has been chosen to produce the same FS radius as the TP example with $E_{\text{SN}} = 10^{51} \text{ erg}$. In all cases, no DSA occurs at the RS.

density and temperature that occur with efficient DSA may make it possible to use observations of thermal X-rays to set limits on the amount of acceleration.

We use as inputs to our thermal models a set of hydrodynamic models in which we vary the ambient magnetic field B_0 , the ambient density n_H , and the acceleration efficiency ϵ_{rel} . The acceleration efficiency, ϵ_{rel} , is defined as the percentage of energy flux crossing the shock (in the shock rest frame) that ends up in relativistic particles, and it is uniquely determined by χ_{inj} . The acceleration efficiency includes particles in the particle distributions downstream from the shock as well as the high-energy particles that escape upstream from the shock. All models are initialized in a similar way typical of Type Ia supernovae: we use an exponential density profile (e.g., Dwarkadas 2000) for the SNR ejecta, an ejecta mass $M_{\text{ej}} = 1.4 M_{\odot}$, and an ejecta kinetic energy $E_{\text{SN}} = 10^{51}$ erg. We assume that the ambient magnetic field and density are uniform and evolve the models for a time t_{SNR} , typically taken to be 500 yr.⁴

In Figure 2 we show the plasma temperature, density, and volume emission measure (i.e., $\sum \rho^2 V$) with varying injection efficiencies for DSA. In all cases, except for the light-weight curve in the top panel, we take $n_H = 0.1 \text{ cm}^{-3}$, $B_0 = 15 \mu\text{G}$, $t_{\text{SNR}} = 500 \text{ yr}$ and $E_{\text{SN}} = 10^{51}$ erg. For the light-weight curve, we use $E_{\text{SN}} = 1.4 \times 10^{51}$ erg with the same values for n_H , B_0 , and t_{SNR} . Other parameters are listed in Table 1 as models A1, B2, D1, and D2.

The three sets of heavy-weight solid curves have strong DSA with $\epsilon_{\text{rel}} \sim 63\%$ at $t_{\text{SNR}} = 500 \text{ yr}$. The dashed curves are for a moderate acceleration efficiency with $\epsilon_{\text{rel}} \sim 36\%$ and the dotted curves are the test-particle limit with negligible energy flux in relativistic particles ($\epsilon_{\text{rel}} \sim 0$). These results clearly demonstrate the two most important effects efficient CR production has on the remnant dynamics: the plasma temperature behind the FS (top panel) drops by nearly a factor of 10 between the efficient acceleration and test-particle examples, and the shock compression (middle panel) immediately behind the FS increases by a factor $7.7/4 \sim 2$.⁵

The quantity $\sum \rho^2 V$ in the bottom panel (where ρ is the shocked plasma density and V is the volume of the shocked plasma), is similar to the emission measure (EM); the thermal X-ray emission is proportional to $\sum \rho^2 V$. The light-weight bar is $\sum \rho^2 V$ for the region between the reverse shock and the contact discontinuity, and the heavy-weight bar is for the region between the forward shock and the contact discontinuity.

An important consequence of efficient DSA is that it results in a smaller forward shock radius at

⁴A remnant age of $t_{\text{SNR}} = 500 \text{ yr}$ is chosen mainly for computational convenience although it allows comparison with some young historical SNRs.

⁵The compression ratios indicated in Table 1 are low compared to what is possible in nonlinear DSA (see, for example, Ellison et al. 2005, for extreme cases with $r_{\text{tot}} \sim 100$). The modest values for r_{tot} obtained here result from a combination of restricting the acceleration efficiency and assuming large upstream fields. As described in Ellison et al. (2005), in the approximations used in our CR-hydro model, large upstream fields result in heating of the shock precursor and reduce the overall acceleration efficiency and r_{tot} .

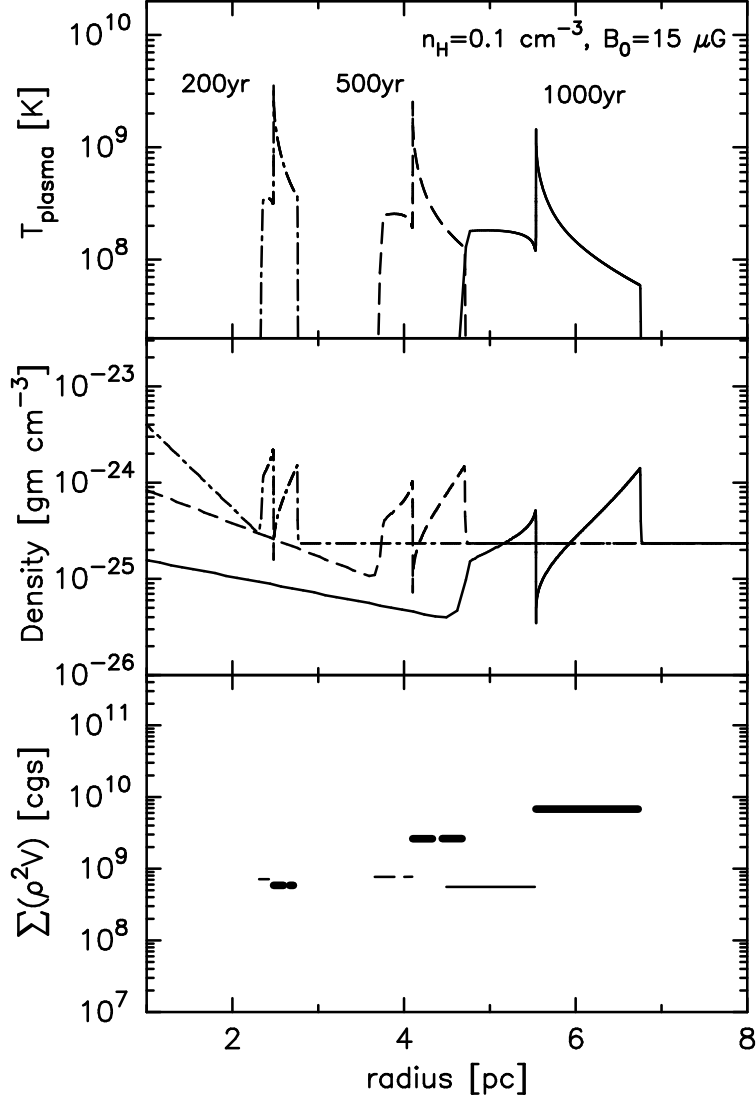


Fig. 3.— Temperature, density, and $\Sigma \rho^2 V$ as in Figure 2. The various sets of curves were calculated at $t_{\text{SNR}} = 200, 500,$ and 1000 yr as indicated. In all examples, $\epsilon_{\text{rel}} \sim 50\%$ at t_{SNR} . The dashed curves are model A3 in Table 1.

a given age as compared to the test-particle limit. A comparison of the FS positions of the heavy-weight solid and dotted curves in Figure 2 shows that the FS radius drops by a factor of $4.6/5 \sim 0.9$ between the test-particle and highly efficient acceleration cases with a corresponding drop in the FS/CD ratio. Such an effect is observed in Tycho’s SNR (Warren et al. 2005), providing strong evidence for efficient particle acceleration in this young remnant. The light-weight solid curve in the top panel has strong DSA ($\epsilon_{\text{rel}} \sim 63\%$), but the supernova explosion energy has been increased from 10^{51} erg (heavy-weight curves) to 1.4×10^{51} erg to obtain the same FS radius as the test-particle case. If efficient DSA occurs and is ignored, systematic errors in estimates for E_{SN} will occur.

In Figure 3 we show the shocked plasma temperature, density, and $\sum \rho^2 V$ at $t_{\text{SNR}} = 200, 500,$ and 1000 yr. These are efficient forward shock acceleration cases with $\epsilon_{\text{rel}} \sim 50\%$ at t_{SNR} . At $t_{\text{SNR}} = 200$ yr, $\sum \rho^2 V$ is slightly higher at the RS, but by 1000 yr, $\sum \rho^2 V$ is almost an order of magnitude higher in the FS. This occurs, of course, because the FS continues to sweep up CSM material as the remnant expands.

Figure 4 shows a similar set of curves, also for $\epsilon_{\text{rel}} \sim 50\%$, only now the age is fixed at 500 yr and n_{H} is varied as shown. As expected, $\sum \rho^2 V$ at the forward shock scales roughly as n_{H}^2 . At the RS, $\sum \rho^2 V$ also shows a correlation with n_{H} but it is considerably weaker than n_{H}^2 .

In addition to modifying the evolution and the temperature of the shocked gas, changes in the compression of the fluid should result in changes in the compression of the magnetic field, implying that the morphology and intensity of synchrotron emission from relativistic electrons will vary strongly with the efficiency of DSA and with the orientation and strength of the magnetic field.⁶ The magnetic field in the CR-hydro model is exactly as described in Ellison & Cassam-Chenai (2005) and we emphasize that the DSA model used here does not explicitly include the magnetic field. What this means is that instead of including the magnetic field self-consistently in determining the shock structure, the far upstream field strength, B_0 , is used to calculate a rate of Alfvén heating in the shock precursor (as described in Berezhko & Ellison 1999) which in turn modifies the subshock compression and overall acceleration efficiency. An ad hoc field compression model is assumed to determine the downstream field (e.g., Ellison & Cassam-Chenai 2005) and this compressed field is used to calculate synchrotron emission.

Significantly, our model does not include magnetic field amplification even though this is now believed to be an important effect in SNR shocks (e.g., Vink & Laming 2003; Völk et al. 2005a). Field amplification, as opposed to simple compression, comes about when backstreaming energetic particles transfer energy to magnetic turbulence to create a nonlinear situation where $\Delta B/B \gg 1$ (Bell & Lucek 2001). Efforts are now underway to incorporate this process into nonlinear models of DSA (i.e., Amato & Blasi 2006; Vladimirov, Ellison, & Bykov 2006; Blasi, Amato, & Caprioli 2006). We do not attempt to model such amplification here, but (in a fashion similar to, for

⁶We note that the orientation of the magnetic field is not included explicitly in our model. As discussed in Ellison & Cassam-Chenai (2005), for the purposes of calculating the evolution of the field, we assume the shocked field is fully turbulent.

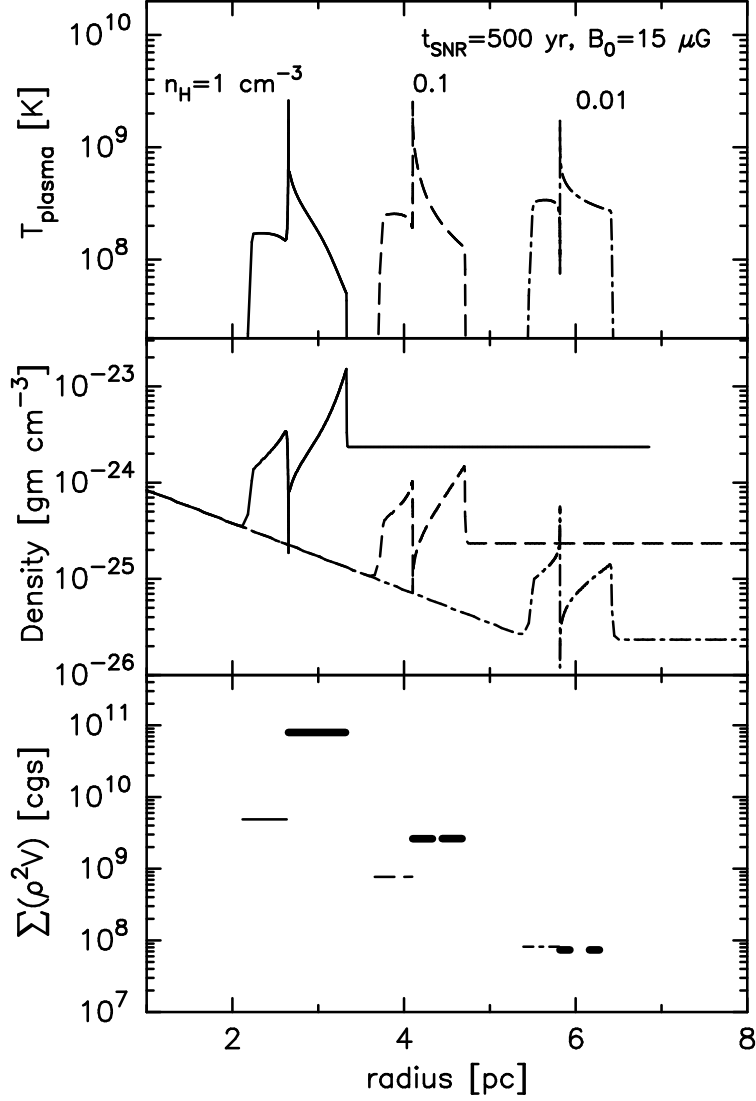


Fig. 4.— Temperature, density, and $\sum \rho^2 V$ as in Figure 2. The various sets of curves were calculated with different n_{H} as indicated. In all cases, $\epsilon_{\text{rel}} \simeq 50\%$. The dashed curves are model A3 in Table 1.

example, Völk et al. 2005a), we investigate the effects of the associated strong postshock magnetic fields by considering the case with a strong ($60 \mu\text{G}$) upstream field which, upon strong compression under conditions of efficient particle acceleration, in some ways mimics the amplification process.

In Figure 5 we show electron and proton spectra for two cases, one with test-particle acceleration, ($\epsilon_{\text{rel}} \sim 0$; dashed curves, top panel) and one with efficient DSA, ($\epsilon_{\text{rel}} \sim 63\%$; solid curves, middle panel). For this example, the specific parameters are not important other than to emphasize that the only difference in input between the two models is the injection efficiency at the forward shock χ_{inj} . The spectra shown are integrated over the region between the CD and FS. Both the spectral curvature and the shift of the thermal peak to lower momenta with efficient DSA are evident. In the bottom panel of Figure 5 are the synchrotron and bremsstrahlung spectra generated by the electron distributions. The two vertical lines show the 1-10 keV range relevant for X-ray observations. The important points to be made here are:

(i) The spectral curvature in the synchrotron emission is far too small to show up in the limited X-ray range, although it is important for matching radio to X-ray fluxes since nonlinear effects increase the X-ray/radio ratio significantly (Baring et al. 1999; Ellison et al. 2001; Berezhko et al. 2002);

(ii) In the models shown, the synchrotron spectral shape in the critical 1-10 keV range is determined by the shape of the turnover in the electron distribution near the maximum momentum. The momentum and shape of this turnover is determined by α_{cut} ,⁷ radiation losses (synchrotron and inverse-Compton losses off the primordial background radiation) and adiabatic expansion as well as the maximum momentum, p_{max} , the shock can produce. Both the rate of radiation losses and p_{max} depend on the momentum dependence of the diffusion coefficient, κ , near p_{max} , which is unknown. To our knowledge, all serious models of SNRs currently in use, including ours, assume that $\kappa \propto p$ at p_{max} , but this need not be the case (see Amato & Blasi 2006; Vladimirov, Ellison, & Bykov 2006; Blasi, Amato, & Caprioli 2006). If κ near p_{max} has a momentum dependence other than $\propto p$, the shape of the synchrotron emission near 1 keV can be substantially modified.

(iii) The bremsstrahlung continua without emission lines in the bottom panel (light-weight curves) illustrate the effects on the thermal emission. First, note that the particle spectra in Figure 5 are “complete” in that they contain all of the mass in the shocked gas. For this example, we assume the ambient plasma is fully ionized hydrogen and helium with 10% helium by number and that $T_{2e} = T_{2p} = T_{2\alpha}$, that is, the shocked plasma of electrons, protons, and α -particles comes into equilibrium immediately behind the shock. In this example, the thermal continuum is dominated by the synchrotron [(heavy curve)/(light curve)] for both the TP and efficient cases. However, the synch/brems ratio at 1 keV drops from $\sim 10^3$ in the efficient case [(heavy solid curve)/(light solid

⁷The parameter α_{cut} is described in detail in Ellison et al. (2004) (see eq. 2 in that paper). Simply stated, when $\alpha_{\text{cut}} = 1$, an exponential turnover is imposed on the particle spectra near p_{max} . This turnover can be important for modeling synchrotron X-rays but the actual shape of the turnover can’t be determined with the semi-analytic code used here.

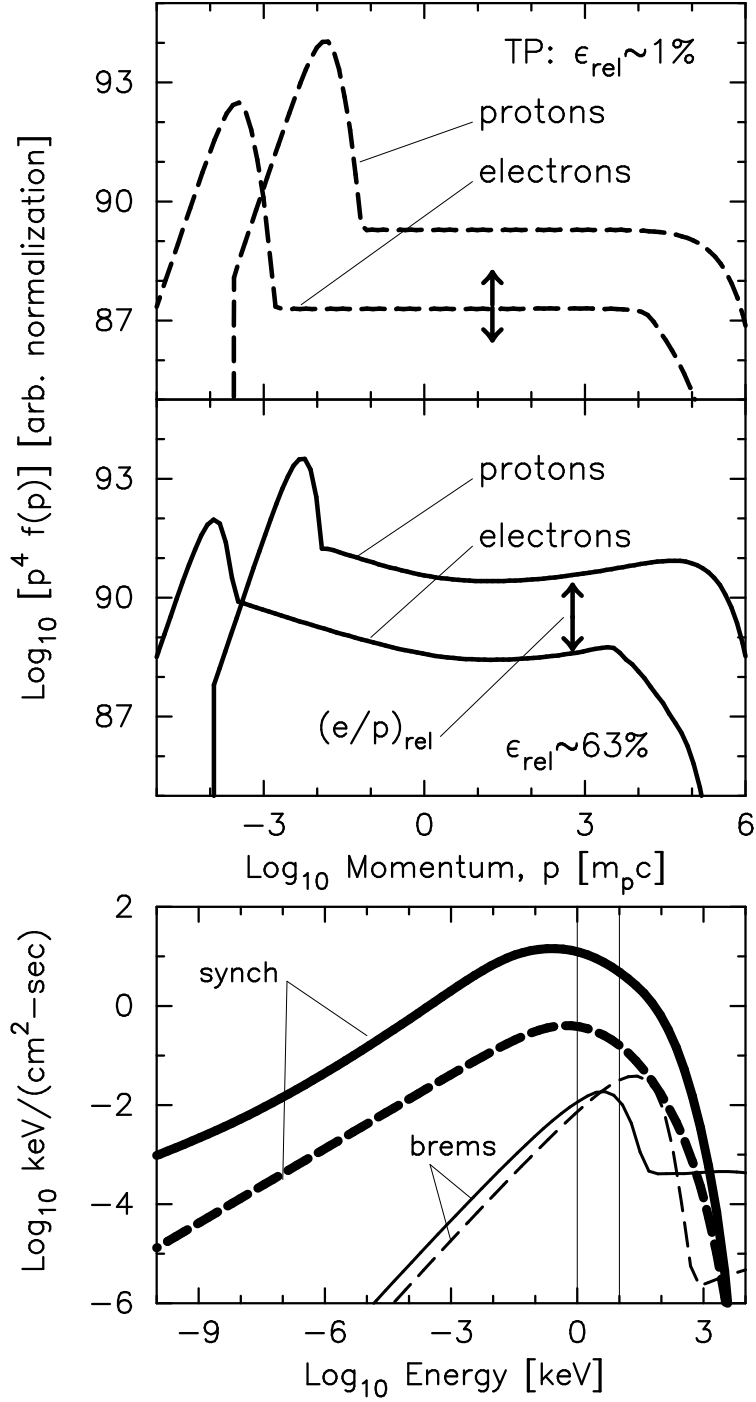


Fig. 5.— The top two panels show electron and proton spectra, $p^4 f(p)$, for TP DSA ($\epsilon_{\text{rel}} \sim 1\%$, dashed curves, \sim model A1) and efficient DSA ($\epsilon_{\text{rel}} \sim 63\%$, solid curves, model D1). The bottom panel shows synchrotron and bremsstrahlung spectra for these two cases: solid curves - efficient DSA, dashed curves - TP. In all cases, $B_0 = 15 \mu\text{G}$ and $n_{\text{H}} = 0.1 \text{ cm}^{-3}$. There is a large variation in the synch/brem ratio in the X-ray range between these two cases. The up-down arrow in the top panel indicates that the normalization of the power law, relative to the thermal distribution, is arbitrary in the test-particle case other than that the power law is low enough to contain an insignificant fraction of the total energy. The up-down arrow in the middle panel shows the arbitrary parameter $(e/p)_{\text{rel}} = 0.01$, typical of the ratio observed in galactic cosmic rays. The thermal electron distributions shown assume instant temperature equilibration with protons behind the shock.

curve)] to ~ 50 in the TP case [(heavy dashed curve)/(light dashed curve)]. The shift to a lower electron temperature with efficient DSA is also evident in the bremsstrahlung curves.

Actual SNRs often show a mixture of thermal and nonthermal X-ray emission (Kepler’s and Tycho’s SNRs show a mixture, whereas in G347.3–0.5, the X-ray emission is wholly nonthermal, e.g., Slane et al. 1999). We now describe how we use the above hydrodynamical models to calculate the thermal X-ray emission which is expected from cosmic-ray modified shocks.

2.2. NEI Model of Thermal Emission

To properly predict the thermal X-ray emission produced by a shock-heated gas, it is necessary to determine the ionization state for each element in the gas. Particularly for the low densities found in SNRs, this ionization state can differ significantly from that expected for a gas in collisional ionization equilibrium at the associated electron temperature of the postshock gas, T_e (Hamilton et al. 1983; Hamilton & Sarazin 1984). The approach to an equilibrium state for the ionization depends upon both the electron density n_e and the time over which the gas has been ionizing (i.e. the time since it was shocked). The non-equilibrium ionization (NEI) state for such an evolving plasma has been calculated by a number of authors (e.g., Hughes & Helfand 1985; Itoh 1979; Borkowski et al. 2001) the latter of whom have implemented the calculation in a routine in the XSPEC software package. Here the ionization state is calculated for given values of the plasma temperature and so-called ionization timescale $\tau = n_e t$, and the ionization values are then coupled to a plasma emissivity code to produce the expected spectrum.

To investigate the X-ray spectra from the shock-heated gas in an SNR under conditions of efficient particle acceleration, we have coupled the values for the evolution of the temperature and density in the postshock gas, determined from hydrodynamical simulations, with the NEI model in XSPEC. Specifically, for a remnant of a given age, we use the values of τ and T_e , along with the volume emission measure $n_e n_H dV / (4\pi D^2)$ for each radial shell from the simulation as input to the NEI model (D is the distance to the remnant). We consider two cases for the heating of the electrons in the postshock region: instant equilibration with the ion temperature, and equilibration through Coulomb collisions (Spitzer 1968). For both cases we include the effects of adiabatic expansion on the temperature components. We note that our line emissivity calculations assume a Maxwellian distribution for the exciting electrons and ignore the possible excitation by superthermal electrons or protons. When particle acceleration is efficient, the low energy particles may, in fact, have a distribution that differs somewhat from a Maxwellian although there is no reason this difference should be significantly more than in the case with inefficient acceleration. More importantly, superthermal particles may contribute to the ionization, particularly for the iron K- α line. These effects are just starting to be considered (e.g., Vink et al. 1997; Porquet et al. 2001) and are beyond the scope of this paper.

The ionization rate for a given species is highly dependent upon the electron temperature. As

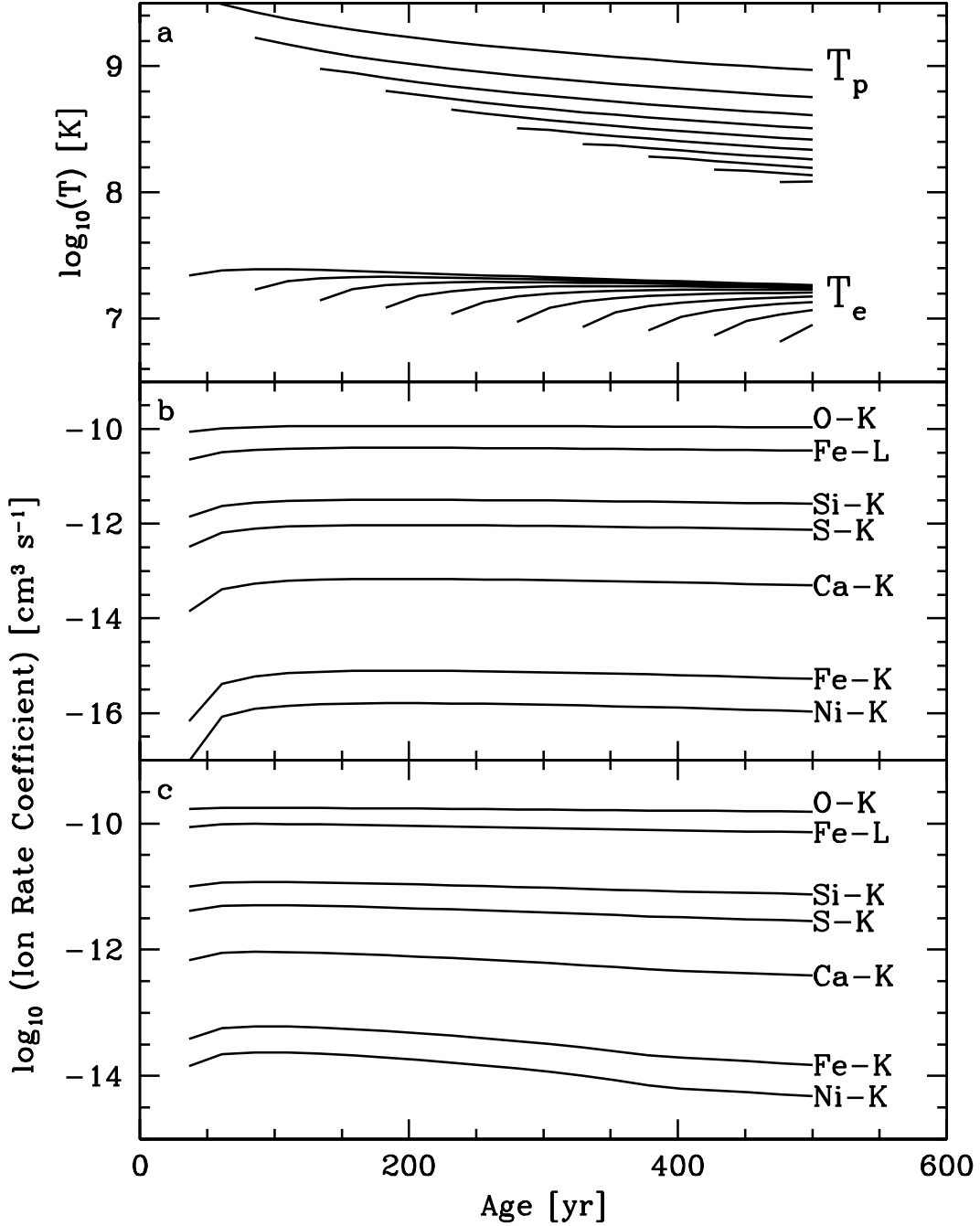


Fig. 6.— The top panel shows the electron and proton temperature evolution for various shells in the region between the CD and FS assuming heating by Coulomb collisions. The left end-point of each line indicates the SNR age at which the shell was formed. The lower two panels show the total K- and L-shell ionization rates for several X-ray emitting ions. Ions such as Mg-K and Ar-K are not shown but have similar profiles. In panels a and c, $n_H = 1 \text{ cm}^{-3}$, $B_0 = 15 \mu\text{G}$, and $\epsilon_{\text{rel}} \simeq 36\%$ (model B3, Table 1). In panel b, $n_H = 0.1 \text{ cm}^{-3}$, $B_0 = 15 \mu\text{G}$, and $\epsilon_{\text{rel}} \simeq 36\%$ (model B2).

shown in the top panel of Figure 6, both the electron and ion temperatures evolve as the SNR ages, due to Coulomb heating of the electrons and adiabatic expansion (cooling) of the mass shell. Therefore, the ionization state at a particular time for any given shell is dependent upon the ionization history in the shell, and is not a simple function of the current temperature and summed τ . While we defer a complete treatment of the ionization directly in the hydrodynamical simulations to a future paper, we find that there is a suitable parameter space over which the ionization rates and temperatures are roughly constant in time (except for when the shell is initially shock heated) and, thus, for which the ionization rates for X-ray emitting ions are roughly constant (panel b in Figure 6). In such a case, the true ionization age of a mass shell is very close to $n_e t_{\text{age}}$, since the ionization versus time is roughly constant. In the cases where the ionization rates are not nearly constant with time (c.f., panel c in Figure 6), the ionization rates for these states (i.e., Ni-K, Fe-K) are well below the ionization rates for the dominant line emitters (e.g., Fe-L). We note that in the case of shocked ejecta, this approximation will no longer be valid, since there will be more free electrons per ion due to the metal rich nature of the plasma, and this number will evolve as the ejecta ionizes. We defer the treatment of the X-ray emission from the reverse shock to a future publication.

XSPEC requires the following inputs: the electron temperature T_e , the ionization age $n_e t$, the ion density n_i , and the shell volume. We assume an arbitrary distance D of 1 kiloparsec. The ion density is related to the hydrodynamical gas density ρ by $n_i = \rho/(\mu m_{\text{amu}})$, where μ is the mean molecular weight for a cosmic abundance plasma, taken here to be 0.6. We then generate a NEI model for each mass shell. The models are summed together to produce an integrated thermal spectrum, such as that shown in Figure 7. These models can then either be folded through an instrument response to produce a simulated spectrum, or added to the nonthermal X-ray spectrum to produce a complete (thermal and nonthermal) X-ray spectrum.⁸

3. RESULTS

Calculations of SNRs including particle acceleration involve a number of parameters. For all of our results here, we assume that the unshocked CSM is uniform (e.g., no pre-SN wind is present), and define the following environmental parameters for our spherically symmetric calculation: (i) initial kinetic energy of the ejecta material, E_{SN} , (ii) mass of the ejecta, M_{ej} , (iii) age of the SNR, t_{SNR} , (iv) proton number density of the unshocked CSM, n_{H} , (v) magnetic field strength of the unshocked CSM, B_0 , and (vi) composition of the CSM.

Parameters and assumptions for the CR-hydro calculation include: (i) the spatial profile for the ejecta material, (ii) the injection efficiency for DSA, χ_{inj} , (iii) the assumption for the scattering

⁸In the future, we intend to produce XSPEC table models from these combined spectra which can then be used to fit X-ray observations of SNR.

mean free path, i.e., $\lambda = \eta_{\text{mfp}} r_g$, (iv) the cutoff parameter for particle spectra near p_{max} , α_{cut} , and (v) the assumption for compression of magnetic field behind the shock. The mean free path and η_{mfp} only enter the calculation in the determination of p_{max} . The maximum momentum is determined when the upstream diffusion length is equal to some fraction of the shock radius or when the acceleration time equals the shock age, whichever gives the lowest p_{max} . For all of the models here, the fraction of the shock radius that truncates the acceleration is 0.05.

Parameters and assumptions for the NEI calculation include: (i) the assumption for electron heating behind the shock, (ii) the evolution of the plasma ionization, and (iii) the chemical composition of the CSM.

In all of the examples that follow, we keep the following parameters and assumptions fixed: $E_{\text{SN}} = 10^{51}$ erg,⁹ $M_{\text{ej}} = 1.4 M_{\odot}$, an exponential density profile for the ejecta mass, $\eta_{\text{mfp}} = 1$, $\alpha_{\text{cut}} = 1$, and for the magnetic field configuration across the shock, we assume that the field is fully turbulent upstream and, following Völk et al. (2002), set the immediate downstream magnetic field

$$B_2 = \sqrt{1/3 + 2r_{\text{tot}}^2/3} B_0 , \quad (1)$$

where r_{tot} is the shock compression ratio.¹⁰

An example product is given in Figure 7 where we show emission in the X-ray energy range for a particular set of parameters. For this illustration we have $n_{\text{H}} = 0.1 \text{ cm}^{-3}$, $B_0 = 15 \mu\text{G}$, and the results are shown at $t_{\text{SNR}} = 500 \text{ yr}$. Here and elsewhere, we only calculate line emission from the forward shock, summed over the region between the FS and contact discontinuity, and do not adjust the spectra for any type of instrument response. We assume a solar composition for the CSM and, most importantly, we assume that the ionization age τ of the shocked CSM is given solely by the product of the final electron density and the age of the mass shell.

In the top panel of Figure 7 we show a test-particle example where no significant population of relativistic particles is produced. The middle and bottom panels show the result for efficient DSA, where χ_{inj} has been chosen so approximately 50% of the shock energy flux goes into relativistic particles, mainly protons.¹¹ The dashed curve in the middle panel is the synchrotron emission produced by TeV electrons. Except for a few strong lines, this dominates over the thermal emission. The bottom panel shows the summed thermal and nonthermal spectra from the middle panel. A direct comparison with the top panel shows the difference that results by changing a single parameter, the assumed efficiency for DSA. For this example, the shocked electrons were heated via Coulomb collisions with the hot, shocked protons.

⁹We use $E_{\text{SN}} = 1.4 \times 10^{51}$ in a single example shown in Figure 2.

¹⁰The details of this assumption and for the evolution of B behind the shock are given in Ellison & Cassam-Chenaï (2005).

¹¹In all of our examples, the efficiency is calculated at the end of the simulation. During earlier times, the instantaneous acceleration efficiency can be greater or less than the stated value.

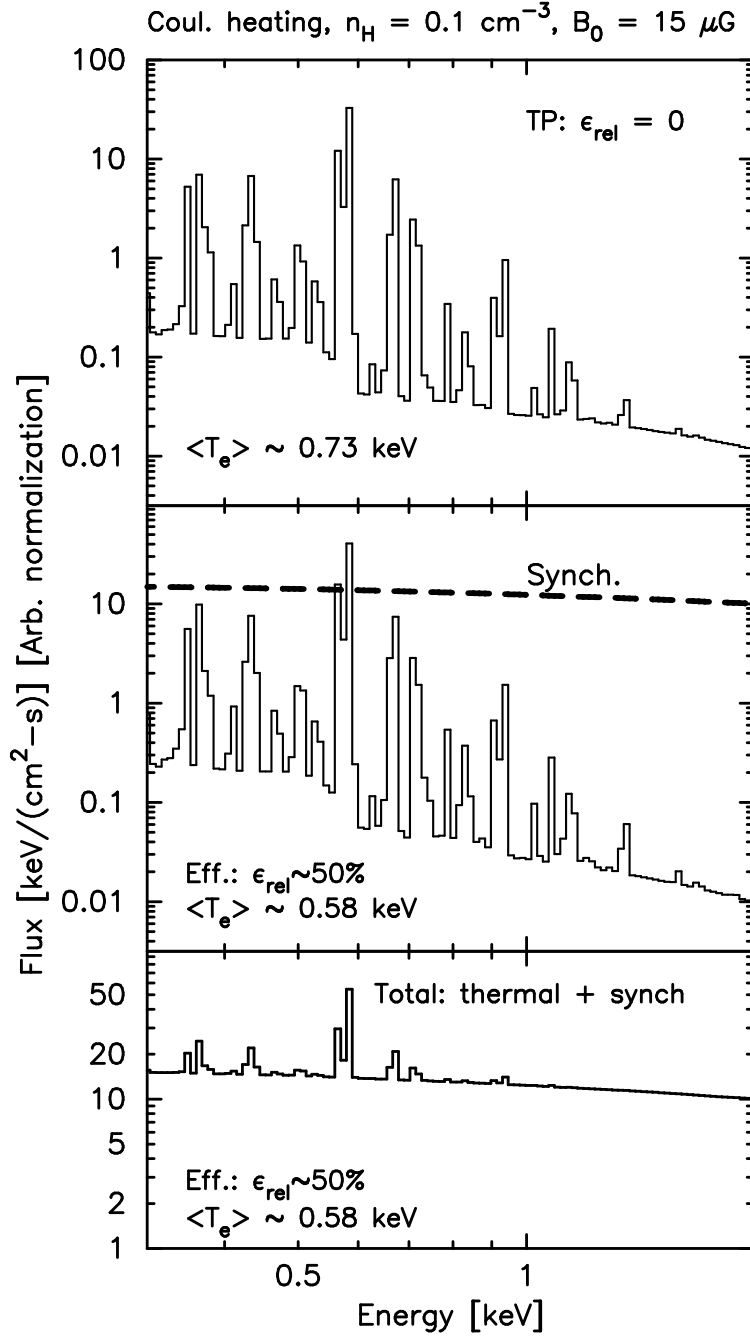


Fig. 7.— The top panel shows thermal X-ray emission with no DSA ($\epsilon_{\text{rel}} = 0$, model A1). The middle and bottom panels show spectra when the percentage of energy placed into relativistic particles by the FS is $\sim 50\%$ (model A3 in Table 1). In all cases, only emission from the FS is shown and it is summed over the region between the FS and CD at $t_{\text{SNR}} = 500 \text{ yr}$. The dashed curve in the middle panel is the synchrotron flux from electrons accelerated by the FS and the bottom panel shows the total emission. For this example, Coulomb heating is assumed for electrons and the mean downstream temperatures are indicated.

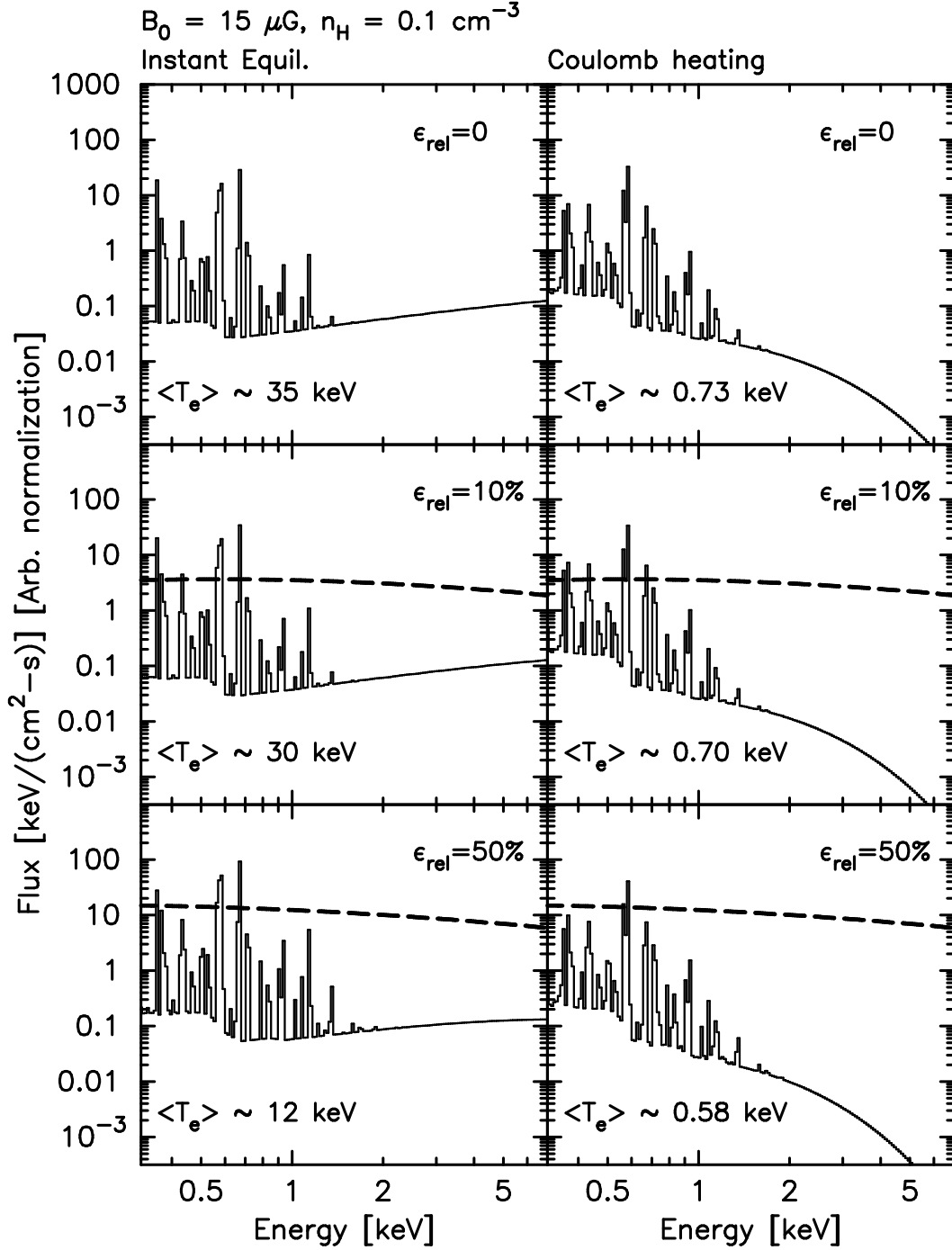


Fig. 8.— Thermal emission for examples where the efficiency of DSA at the FS is varied as indicated. The top panels are model A1, the middle panels are model A2, and the bottom panels are model A3 in Table 1. The emission is summed for the region between the CD and FS and emission from the RS is not included. The dashed curve in each panel is the synchrotron emission from electrons accelerated at the FS. Panels on the left assume instant equilibration between electrons and protons and panels on the right assume Coulomb heating of electrons. All parameters for the various models are identical other than ϵ_{rel} and the electron heating.

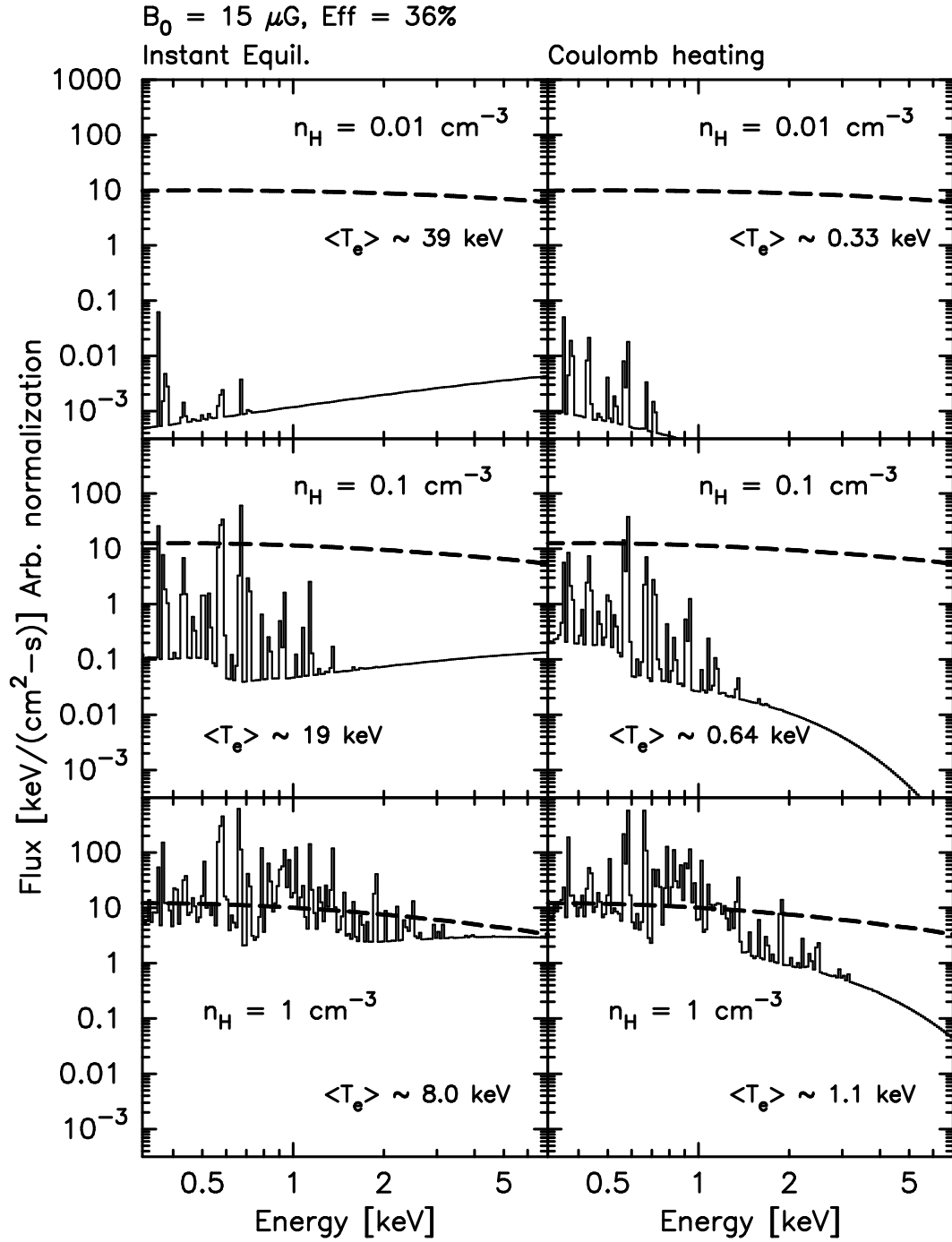


Fig. 9.— Examples similar to Figure 8 where ϵ_{rel} is set at 36% and n_{H} is varied as indicated. The top panels are model B1, the middle panels are model B2, and the bottom panels are model B3 in Table 1.

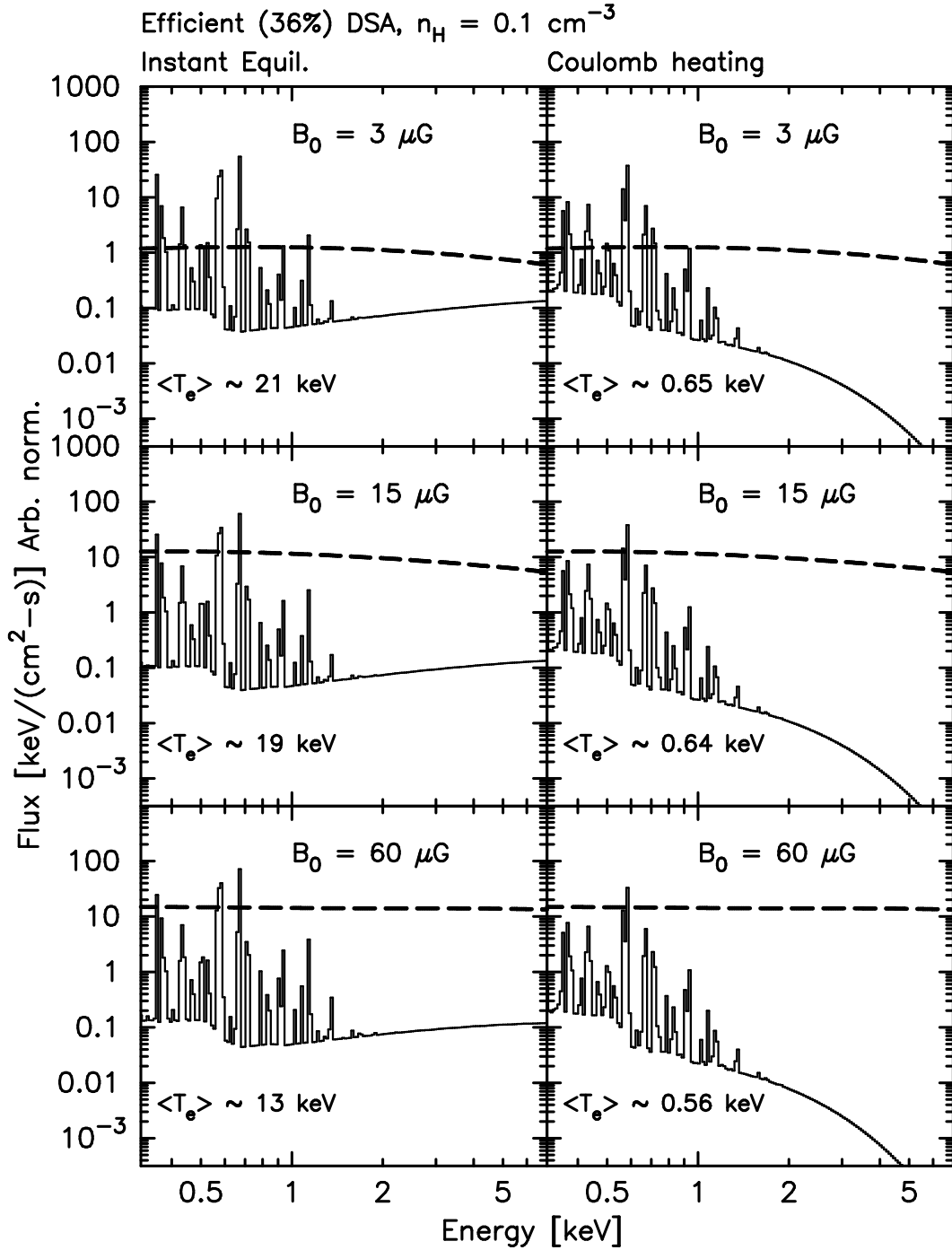


Fig. 10.— Examples similar to Figure 8 where ϵ_{rel} is set at 36%, $n_H = 0.1 \text{ cm}^{-3}$ and the unshocked magnetic field is varied as indicated. The top panels are model C1, the middle panels are model C2, and the bottom panels are model C3 in Table 1.

In Figures 8–10 we show results for models A, B, and C in Table 1. We present the results for the two extremes for electron heating (instant equilibration and Coulomb heating) to stress the obvious differences in the thermal continuum which arise from assuming high electron temperatures. We also vary the acceleration efficiency, ϵ_{rel} , the CSM density, n_{H} , and the magnetic field, B_0 . In Figure 8, we have varied ϵ_{rel} between 0 and 50% while keeping $B_0 = 15 \mu\text{G}$ and $n_{\text{H}} = 0.1 \text{ cm}^{-3}$. Figure 9 shows the effects of varying the density n_{H} while holding ϵ_{rel} and B_0 constant. Finally, in Figure 10 we vary the magnetic field while holding ϵ_{rel} and n_{H} constant. In these figures we plot the nonthermal synchrotron emission as a dashed line and the thermal spectrum as a solid line but do not plot the summed spectrum.

We chose to focus mainly on varying the ambient density, acceleration efficiency, and magnetic field because these parameters have a large influence on the SNR evolution. Increasing the upstream density results in higher volume emission measures and thus higher thermal continua. Increasing the acceleration efficiency changes the equation of state of the shocked CSM resulting in lower post shock plasma temperatures and higher densities. Finally, varying the upstream magnetic field strength influences the acceleration process because it is assumed in our model that energy in shock-accelerated particles in the precursor can be transferred into magnetic turbulence and then into heat. This heating of the precursor weakens the subshock and results in less efficient particle acceleration (see Berezhko & Ellison 1999, for a full discussion). For the cases shown in Figure 10, the injection efficiency, χ_{inj} has been adjusted to produce $\epsilon_{\text{rel}} \simeq 36\%$ as B_0 is changed.

General results from Figures 8, 9, and 10 include:

- (i) synchrotron dominates thermal emission except for the TP examples (top panels in Figure 8) and the $n_{\text{H}} = 1 \text{ cm}^{-3}$ examples in the lower panels in Figure 9.
- (ii) In the TP case (top panels in Figure 8), the differences between instant equilibration and Coulomb heating are large, with the average electron temperature for instant equilibration $\sim 35 \text{ keV}$ and only $\sim 0.73 \text{ keV}$ for Coulomb heating. However, once synchrotron becomes important with $\epsilon_{\text{rel}} \gtrsim 10\%$, the signature of electron heating is difficult to discern against the synchrotron continuum except for high n_{H} (i.e., the $n_{\text{H}} = 1 \text{ cm}^{-3}$ cases in Figure 9).
- (iii) The cases involving instantaneous equilibration produce models with anomalously high electron temperatures, even when DSA is efficient. While these simulations cannot rule out instantaneous electron heating as we are not comparing them to observations of SNR forward shocks, fits to X-ray spectra do not generally predict such high electron temperatures in these regions.

In the top panel of Figure 11 we show the electron and proton spectra for the three instant equilibration examples of Figure 10. The bottom panel shows the synchrotron spectra produced by these electrons. The three cases have $\epsilon_{\text{rel}} \simeq 36\%$ even though the proton spectra look quite different. The major reason for this is that ϵ_{rel} includes the energy in particles that escape upstream from the shock and which is not included in the plotted spectra. The spectra shown are summed over the interaction region and the acceleration efficiency varies during the evolution of the remnant.

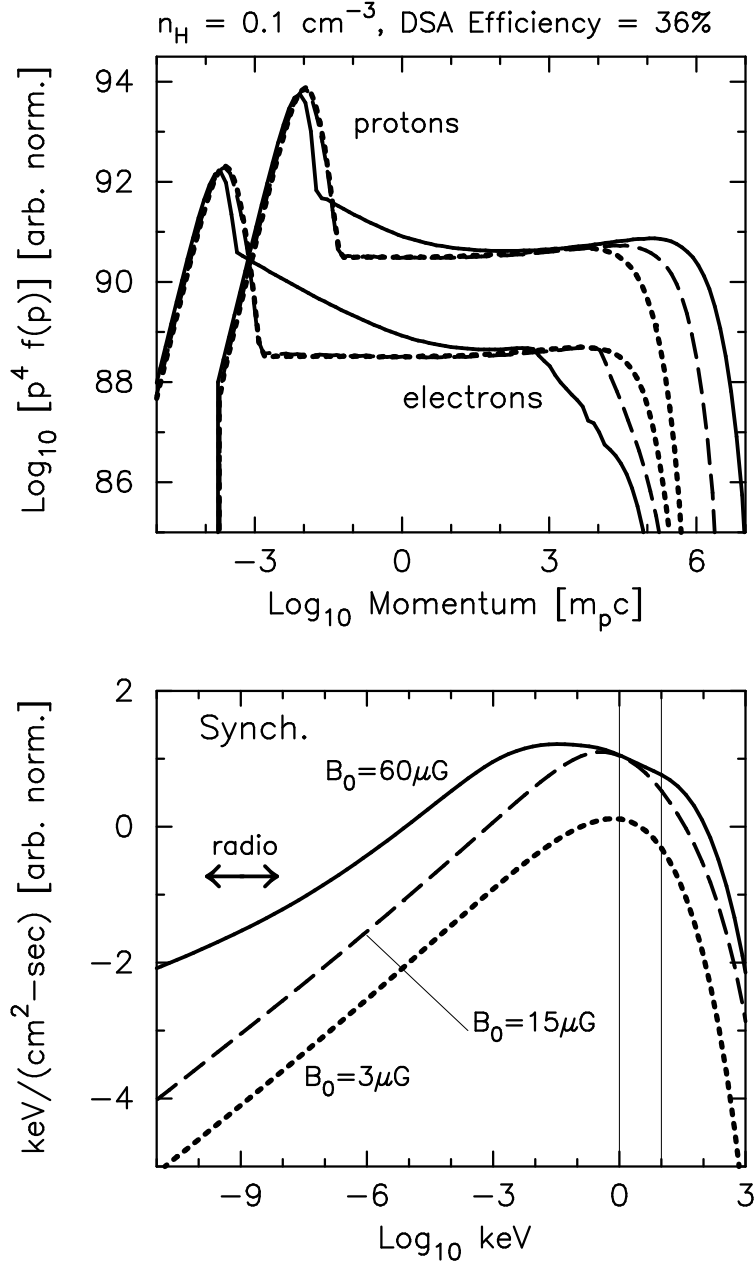


Fig. 11.— The top panel shows particle spectra summed over the SNR at the end of the simulation, i.e., $t_{\text{SNR}} = 500 \text{ yr}$. The bottom panel shows the synchrotron emission from these electrons. All models have the input same parameters except for B_0 which is $3 \mu\text{G}$ for the dotted curves (model C1), $15 \mu\text{G}$ for the dashed curves (model C2), and $60 \mu\text{G}$ for the solid curves (model C3).

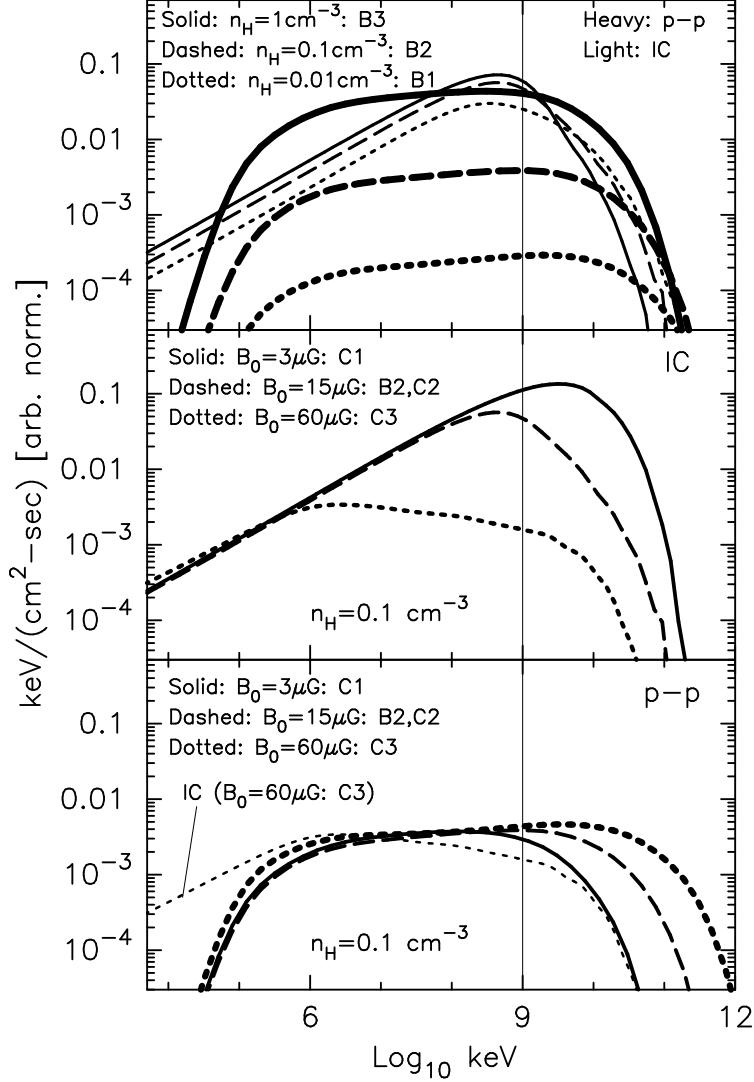


Fig. 12.— Pion-decay and inverse-Compton emission for a range of n_H and B_0 . In the top panel, the heavy-weight curves are pion-decay, the light-weight curves are inverse-Compton, and $\epsilon_{\text{rel}} = 36\%$ and $B_0 = 15 \mu\text{G}$ in all cases. The strong dependence of pion-decay on ambient density n_H is evident. The middle panel shows IC and the bottom panel shows pion-decay for $n_H = 0.1 \text{cm}^{-3}$ with B_0 varying from $3 \mu\text{G}$ (solid curves) to $15 \mu\text{G}$ (dashed curves) to $60 \mu\text{G}$ (dotted curves). For comparison to the π^0 , we show in the bottom panel the IC emission for $B_0 = 60 \mu\text{G}$ (light-weight dotted curve). The particle distributions producing the emission in the bottom two panels are those shown in the top panel of Figure 11.

As B_0 increases, the maximum proton momentum increases in approximate proportion to B_0 .¹² The maximum electron energy decreases with B_0 , however, because synchrotron losses become more severe. The break in the electron spectrum for the $B_0 = 60 \mu\text{G}$ case near $10^3 m_p c$ (solid curves) results because strong radiation losses lower p_{max} for shells shocked early-on. When all shells are added together at t_{SNR} , a steep region spanning several decades in momentum results and this produces a relatively flat region in the X-ray synchrotron spectrum shown in the bottom panel. In the 1–10 keV X-ray energy range, the synchrotron flux varies by nearly an order of magnitude between $B_0 = 3$ and $15 \mu\text{G}$, but the shape is almost indistinguishable.

The GeV-TeV electrons produce inverse-Compton emission as well as synchrotron radiation, and the protons accelerated by the FS interact and produce GeV-TeV photons via proton-proton collisions and pion-decay. In the top panel of Figure 12 we compare the inverse-Compton and pion-decay emission for the examples shown in Figure 9 where n_{H} varies and $B = 15 \mu\text{G}$. As expected, the overall pion-decay flux increases more rapidly with n_{H} than the inverse-Compton flux. At 1 TeV, the ratio $(\text{pion/IC})_{1\text{TeV}}$ is 0.01 for $n_{\text{H}} = 0.01 \text{ cm}^{-3}$, 0.08 for $n_{\text{H}} = 0.1 \text{ cm}^{-3}$, and 0.65 for $n_{\text{H}} = 1 \text{ cm}^{-3}$. It is noteworthy that in order to obtain $(\text{pion/IC})_{1\text{TeV}} > 1$ densities greater than 1 cm^{-3} are required. At energies below $\sim 100 \text{ GeV}$, the pion-decay emission for $n_{\text{H}} = 1 \text{ cm}^{-3}$ becomes stronger than the inverse-Compton as it does at energies above a few TeV. The energy range that will be explored by the Large Area Telescope (LAT) on GLAST (20 MeV–300 GeV) should allow a clear differentiation between emission processes in this case.

In the bottom two panels of Figure 12 we show the IC and pion-decay emission for the particle spectra shown in the top panel of Figure 11. The radiation losses caused by the large magnetic field (dotted curves: $B_0 = 60 \mu\text{G}$ and $B_2 = 310 \mu\text{G}$), combined with the remnant evolution, produce a break in the IC emission in the GeV–TeV range. A comparison of the light- and heavy-weight dotted curves in the bottom panel shows that the shapes of the IC and π^0 components are less distinct than with lower fields and this may make it more difficult to distinguish these components. When B_0 is large, however, the pion-decay emission extends to much higher energy and combining the observations of GLAST and ground-based air-Cherenkov telescopes will help in distinguishing between the hadronic and leptonic scenarios. Currently, HESS spectra of SNRs roughly span the energy range 0.1 – 10 TeV and above 1 TeV the difference between the two dotted curves in the bottom panel becomes significant.

4. DISCUSSION AND CONCLUSIONS

The X-ray emission from SNR shocks is generally a mixture of thermal continuum and line emission, and nonthermal continuum. These components are connected through the particle

¹²We note that this simple scaling is almost certain not to hold if magnetic field amplification is considered. A full discussion is beyond the scope of this paper but preliminary work (Amato & Blasi 2006; Vladimirov, Ellison, & Bykov 2006; Blasi, Amato, & Caprioli 2006) suggests that p_{max} will not increase in proportion to B_0 .

acceleration process, but are generally modeled independently. Here we present the first results from an ongoing project to model the X-ray emission in a fully self-consistent manner with the SNR hydrodynamics and broad-band continuum radiation. The problem is a complicated one with a number of uncertain parameters both for the model and the environment. In order to simplify our presentation and to emphasize the important aspects of our model, we concentrate on emission from the outer blast wave (forward shock) and use approximate techniques to model the non-equilibrium ionization in the interaction region between the contact discontinuity and FS.

The results we present are intended to show broadly how the X-ray emission depends on important parameters including the shock acceleration efficiency, ϵ_{rel} , the unshocked CSM proton number density, n_{H} , the magnetic field strength, B_0 , and two extremes of electron heating: instant equilibration and Coulomb heating. In summary, our results for the forward shock show:

(i) Synchrotron emission from relativistic electrons becomes important, and even dominant, in the X-ray energy range for modest acceleration efficiencies over a wide range of CSM densities and magnetic fields. As shown in Figures 8, 9, and 10, only TP cases or those with large $n_{\text{H}} \sim 1 \text{ cm}^{-3}$ show thermal line emission clearly dominant over synchrotron emission. Once $\epsilon_{\text{rel}} \gtrsim 10\%$ synchrotron emission is likely to be important for typical SNR parameters.

(ii) The two extremes for electron heating, instant equilibration and Coulomb heating, produce very different thermal spectra as expected. However, it may be difficult to distinguish these in cases where synchrotron radiation dominates.

(iii) Changes in the ambient magnetic field, B_0 , have a large effect on the synchrotron emission in the X-ray range but these effects tend to saturate in terms of overall flux for large B_0 (bottom four panels in Figure 10). The saturation is a result of the fact that large magnetic fields tend to dampen DSA, at least in the approximate DSA model used here.

(iv) As has been recognized for some time, broad-band models and fits are critical for constraining important SNR parameters; we illustrate this in Figures 11 and 12. In homogeneous nonlinear models, such as ours, changes in parameters that modify emission in one energy band will modify emission from radio to TeV γ -rays. Thus, if large magnetic fields produce hard synchrotron spectra in the X-ray band, these same electrons will produce strong radio emission (bottom panel of Figure 11). If particular ambient densities are required to match thermal X-ray observations, these densities strongly influence the $(\text{pion/IC})_{1\text{TeV}}$ ratio (top panel in Figure 12).

(v) As has been emphasized by many authors, direct evidence for CR ion production in SNRs can come from identifying pion-decay emission at GeV–TeV energies. The interpretation of GeV–TeV observations is complicated however because pion-decay photons from proton-proton interactions and IC emission from TeV electrons scattering off of the cosmic background radiation are expected to produce similar fluxes in the GeV-TeV energy range. It is generally assumed that the shape of pion-decay emission is sufficiently different from that of IC to allow a clear differentiation if a large enough energy range is sampled. In the bottom two panels of Figure 12 we show spectra for a range of B_0 and it is clear that the shapes of the IC spectra in the GeV-TeV region depend

fairly strongly on the magnetic field with the $B_0 = 60 \mu\text{G}$ case (where strong radiation losses and evolution produce a break in the underlying electron spectrum) closely mimicking the pion-decay shape in the 1 GeV–1 TeV range. For large fields, however, significant differences in shape and intensity occur at both lower and higher energies highlighting the importance of air-Cherenkov observations above 1 TeV and for future observations by GLAST below 1 GeV.

The model we have presented is, we believe, the first to self-consistently determine the synchrotron continuum with thermal emission in the X-ray energy range. However, a number of steps remain before realistic models are produced that can be used to interpret X-ray observations. These steps include: (i) modeling of the reverse shock, which requires an accurate description of the ejecta composition and spatial distribution; (ii) calculating the ionization rates for material behind both the forward and reverse shocks, including time dependence and variations in temperature and electron density; (iii) line-of-sight projections; and (iv) incorporating the effects of the instrument response for general X-ray spectra without restriction to specific models such as those currently used in, for example, XSPEC.

D.C.E is grateful for support from a NASA ATP grant (ATP02-0042-0006) and a NASA LTSA grant (NNH04Zss001N-LTSA), P.O.S. acknowledges support from NASA contract NAS8-39073, and the work of P.B. was partially funded through grant Prin2004.

REFERENCES

- Aharonian, F. A., Akhperjanian, A. G., Aye, K.-M., et al. 2004, *Nature*, 432, 75
- Albert, J., Aliu, E., Anderhub, H., et al. 2006, *ApJ*, 637, L41
- Allen, G. E., Houck, J. C., & Sturmer, S. J. 2005, in *X-Ray and Radio Connections* (eds. L.O. Sjouwerman and K.K Dyer) Published electronically by NRAO, <http://www.aoc.nrao.edu/events/xraydio> Held 3-6 February 2004 in Santa Fe, New Mexico, USA, (E4.07) 6 pages
- Amato, E. & Blasi, P. 2005, *MNRAS*, 364, L76
- Amato, E. & Blasi, P. 2006, *MNRAS*, 371, 1251
- Baring, M. G., Ellison, D. C., Reynolds, S. P., Grenier, I. A., & Goret, P. 1999, *ApJ*, 513, 311
- Bell, A. R. & Lucek, S. G. 2001, *MNRAS*, 321, 433
- Berezhko, E. G. & Ellison, D. C. 1999, *ApJ*, 526, 385
- Berezhko, E. G., Ksenofontov, L. T., & Völk, H. J. 2002, *A&A*, 395, 943
- Blasi, P. 2002, *Astroparticle Physics*, 16, 429
- Blasi, P. 2004, *Astroparticle Physics*, 21, 45
- Blasi, P., Amato, E., & Caprioli, D. 2006, *ArXiv Astrophysics e-prints*
- Blasi, P., Gabici, S., & Vannoni, G. 2005, *MNRAS*, 361, 907
- Borkowski, K. J., Lyerly, W. J., & Reynolds, S. P. 2001, *ApJ*, 548, 820
- Boulares, A. & Cox, D. P. 1988, *ApJ*, 333, 198
- Chevalier, R. A. 1983, *ApJ*, 272, 765
- Decourchelle, A., Ellison, D. C., & Ballet, J. 2000, *ApJ*, 543, L57
- DeLaney, T., Koralesky, B., Rudnick, L., & Dickel, J. R. 2002, *ApJ*, 580, 914
- Dorfi, E. A. & Bohringer, H. 1993, *A&A*, 273, 251
- Dwarkadas, V. V. 2000, *ApJ*, 541, 418
- Eichler, D. 1984, *ApJ*, 277, 429
- Ellison, D. C., Berezhko, E. G., & Baring, M. G. 2000, *ApJ*, 540, 292
- Ellison, D. C. & Cassam-Chenaï, G. 2005, *ApJ*, 632, 920

- Ellison, D. C., Decourchelle, A., & Ballet, J. 2004, *A&A*, 413, 189
- Ellison, D. C., Decourchelle, A., & Ballet, J. 2005, *A&A*, 429, 569
- Ellison, D. C., Slane, P., & Gaensler, B. M. 2001, *ApJ*, 563, 191
- Gotthelf, E. V., Koralesky, B., Rudnick, L., et al. 2001, *ApJ*, 552, L39
- Hamilton, A. J. S., Chevalier, R. A., & Sarazin, C. L. 1983, *ApJS*, 51, 115
- Hamilton, A. J. S. & Sarazin, C. L. 1984, *ApJ*, 284, 601
- Heavens, A. F. 1984, *MNRAS*, 211, 195
- Hughes, J. P. & Helfand, D. J. 1985, *ApJ*, 291, 544
- Itoh, H. 1979, *PASJ*, 31, 541
- Jones, F. C. & Ellison, D. C. 1991, *Space Science Reviews*, 58, 259
- Jones, T. J., Rudnick, L., DeLaney, T., & Bowden, J. 2003, *ApJ*, 587, 227
- LeBohec, S., Atkins, R. W., Badran, H. M., et al. 2006, *Journal of Physics Conference Series*, 47, 232
- Porquet, D., Arnaud, M., & Decourchelle, A. 2001, *A&A*, 373, 1110
- Reynolds, S. P. & Ellison, D. C. 1992, *ApJ*, 399, L75
- Rho, J., Dyer, K. K., Borkowski, K. J., & Reynolds, S. P. 2002, *ApJ*, 581, 1116
- Slane, P., Gaensler, B. M., Dame, T. M., et al. 1999, *ApJ*, 525, 357
- Spitzer, L. 1968, *Diffuse matter in space* (New York: Interscience Publication, 1968)
- Tanimori, T., Hayami, Y., Kamei, S., et al. 1998, *ApJ*, 497, L25+
- Völk, H. J., Berezhko, E. G., Ksenofontov, L. T., & Rowell, G. P. 2002, *A&A*, 396, 649
- Vink, J., Kaastra, J. S., & Bleeker, J. A. M. 1997, *A&A*, 328, 628
- Vink, J. & Laming, J. M. 2003, *ApJ*, 584, 758
- Vladimirov, A., Ellison, D. C., & Bykov, A. 2006, *ApJ*, 652, 1246
- Völk, H. J., Berezhko, E. G., & Ksenofontov, L. T. 2005a, *A&A*, 433, 229
- Warren, J. S., Hughes, J. P., Badenes, C., et al. 2005, *ApJ*, 634, 376